NANO · MICRO small
www.small-journal.com

Optimizing Interplanar Spacing, Oxygen Vacancies and Micromorphology via Lithium-Ion Pre-Insertion into Ammonium Vanadate Nanosheets for Advanced Cathodes in Aqueous Zinc-Ion Batteries

Ji Chen, Yijun Zhai, Yangjie Li, Xiaoyue Zhang, Xiaoqin Zhang, Yuxiang Chen, Yuxiao Zeng, Xingqiao Wu, Qiaoji Zheng, Kwok-Ho Lam, Xin Tan,* and Dunmin Lin**

Ammonium vanadates, featuring an N—H···O hydrogen bond network structure between NH_4^+ and V—O layers, have become popular cathode materials for aqueous zinc-ion batteries (AZIBs). Their appeal lies in their multi-electron transfer, high specific capacity, and facile synthesis. However, a major drawback arises as Zn^{2+} ions tend to form bonds with electronegative oxygen atoms between V—O layers during cycling, leading to irreversible structural collapse. Herein, Li^+ pre-insertion into the intermediate layer of $NH_4V_4O_{10}$ is proposed to enhance the electrochemical activity of ammonium vanadate cathodes for AZIBs, which extends the interlayer distance of $NH_4V_4O_{10}$ to 9.8 Å and offers large interlaminar channels for Zn^{2+} (de)intercalation. Moreover, Li^+ intercalation weakens the crystallinity, transforms the micromorphology from non-nanostructured strips to ultrathin nanosheets, and increases the level of oxygen defects, thus exposing more active sites for ion and electron transport, facilitating electrolyte penetration, and improving electrochemical kinetics of electrode. In addition, the introduction of Li^+ significantly reduces the bandgap by 0.18 eV, enhancing electron transfer in redox reactions. Leveraging these unique advantages, the Li^+ pre-intercalated $NH_4V_4O_{10}$ cathode exhibits a high reversible capacity of 486.1 mAh g^{-1} at 0.5 A g^{-1} and an impressive capacity retention rate of 72% after 5,000 cycles at 5 A g^{-1}.

1. Introduction

In recent years, rechargeable aqueous metal-ion batteries (e.g., Zn^{2+}, Mg^{2+}, and Al^{3+}) have emerged as promising alternatives to traditional lithium-ion batteries with organic electrolytes. This is attributed to their attractive characteristics, including intrinsic safety, cost-effectiveness, and superior ion conductivity.[1–4] Aqueous zinc-ion batteries (AZIBs) have stood out recently to be potential contenders for the future generation of grid-scale energy storage devices. The unique benefits of zinc metal anodes, such as good electrochemical stability, high theoretical mass and volume capacities (820 mAh g^{-1} and 5854 mAh cm^{-3}) and low redox potential (−0.76 V vs Standard Hydrogen Electrode), contribute to their prominence.[1,5–10] However, the development of cathode materials that strike a satisfactory equilibrium among capacity, rate performance, and cycle stability remains a major challenge on the path to the commercialization of AZIBs.[11–14]

J. Chen, Y. Zhai, Y. Li, X. Zhang, Y. Chen, Y. Zeng, Q. Zheng, D. Lin
College of Chemistry and Materials Science
Sichuan Normal University
Chengdu 610066, China
E-mail: ddmd222@sicnu.edu.cn

X. Zhang, X. Wu, X. Tan
Institute for Carbon Neutralization
College of Chemistry and Materials Engineering
Wenzhou University
Wenzhou, Zhejiang 325035, China
E-mail: xintan@wzu.edu.cn

K.-H. Lam
Centre for Medical and Industrial Ultrasonics
James Watt School of Engineering
University of Glasgow
Glasgow G12 8QQ, Scotland
E-mail: kwokho.lam@glasgow.ac.uk

The ORCID identification number(s) for the author(s) of this article can be found under https://doi.org/10.1002/smll.202309412

DOI: 10.1002/smll.202309412

Recently, various cathode materials with different structures for AZIBs have been explored, such as vanadium-based compounds,[15–20] manganese-based compounds,[21–23] Prussian blue analogs,[24,25] sodium superionic conductor (NASICONs) type compounds,[26–28] and chalcogenide compounds,[29,30] Among them, $NH_4V_4O_{10}$, featuring stacked V_4O_{10} units along the a-axis, establishes a stable bilayered structure through sharing edges of vanadium octahedra.[16,31,32] Its broad appeal stems from the robust interaction between NH_4^+ ion and oxygen atom between V—O layers, multivalent states of vanadium, and extensive pathways facilitating Zn^{2+} ion transport.[31,33] Besides, NH_4^+ has a large ionic radius (1.43 Å) and a low molar mass (18 g mol^{-1}), which could provide high mass and volume specific capacities when acting as a pre-inserted layer ion.[34] However, the strong electrostatic attraction between the small-radius Zn^{2+} (0.76 Å) and the highly electronegative oxygen atoms poses a challenge Zn^{2+} ions readily associate with these highly electronegative oxygen atoms within the V—O layers. This interaction, occurring during frequent charging and discharging, induces substantial stress within the core structure, leading to an irreversible structural collapse.[14,35,36] In addition, the $NH_4V_4O_{10}$ has inherent poor conductivity as well as limited active sites, inducing poor electrochemical kinetics.[37–39] Therefore, many strategies, including topography control, defect engineering and pre-intercalation, have been used to boost the dynamics and structural stability of the $NH_4V_4O_{10}$. For example, Li et al. prepared a 3D flower-like structured $NH_4V_4O_{10}$ nanoribbon by a microwave-assisted hydrothermal method,[16] which effectively improves the intercalation kinetics of Zn^{2+}. He et al. synthesized $NH_4V_4O_{10-x}{\cdot}nH_2O$ with oxygen defect,[32] and found that the oxygen vacancy in the crystal framework could not only reduce the Zn^{2+} diffusion energy barrier, but also inhibit the solubilization of vanadium and improve the structural stability (the specific capacity is 343.7 mAh g^{-1} after 100 cycles at 0.1 A g^{-1}). Xu et al. developed a self-engaged method to design C_3N_4 pillared $NH_4V_4O_{10}$,[40] which creates more oxygen vacancies to accelerate the Zn^{2+} diffusion kinetics, providing a high specific capacity of 370 mAh g^{-1} at 0.5 A g^{-1}. Furthermore, various recent researches have indicated that metal cations, such as K^+, Na^+, Mg^{2+}, can be introduced into the interlayers of the $NH_4V_4O_{10}$ to enhance the stability of the layered structure by strengthening ionic bonds. As an illustration, Zhang et al. embedded K^+ into the $NH_4V_4O_{10}$ interlayers,[41] which partially replaces NH_4^+ by K^+, alleviating irreversible deamination and maintaining structural integrity during ion insertion/extraction and thus obtaining ammonium potassium vanadate with an enhanced discharge capacity of 464 mAh g^{-1} at 0.1 A g^{-1}. Su et al. pre-inserted Na^+ and H_2O molecules into $NH_4V_4O_{10}$,[42] thereby reducing the electrostatic repulsion originating from Zn^{2+} insertion/removal and stabilizing the layer structure of the material, and the NVO-Na cathode exhibits an remarkable specific capacity of 400.2 mAh g^{-1} at 0.1 A g^{-1}. Among various alkali metal cations (Li^+, Na^+, and K^+), Li^+ has the smallest molar mass, which suggests the potential for achieving a more ideal discharge capacity when introduced as a pre-intercalated substance between $NH_4V_4O_{10}$ layers. Besides, Li^+ has the greatest electronegativity, which may be anticipated to form strong Li—O bonds with structural oxygen atoms, effectively increasing the stability of layered structures and inhibiting irreversible structural damage during cycling. In addition, owing to the smaller radius of the Li^+ ion (0.76 Å) compared to the NH_4^+ ion (1.43 Å), the hydration radius of Li^+ is larger. Consequently, the introduction of Li^+ tends to decrease the grain growth rate, leading to a noticeable change in morphology.[43,44] The low-valence doping of Li^+ would induce the formation of holes on the lattice oxygen simultaneously, triggering the formation of oxygen vacancies.[45] Therefore, pre-intercalation of Li^+ into $NH_4V_4O_{10}$ can be reasonably expected to modulate the crystal structure and adjust morphology, ultimately leading to an enhancement in the electrochemical performance of the $NH_4V_4O_{10}$ cathode.

Herein, we have constructed $NH_4V_4O_{10}$-based ultra-thin nanosheets by Li^+ intercalation as the cathode for AZIBs. The pre-intercalated Li^+ is used as an interlayer "pillar" ion to effectively enhance the structural stability. Besides, the introduction of Li^+ serves to increase the interlayer spacing within the material, thereby promoting the smooth passage of Zn^{2+} channels. Simultaneously, Li^+ intercalation weakens the crystallinity of the material, leading to the optimization of micromorphology into ultrathin nanosheets. This process induces abundant oxygen defects to enhance the conductive properties of the material and facilitate the electron transfer during redox reactions. Moreover, density of states (DOS) calculations confirm the enhancement in the electronic conductivity of the cathode material after the introduction of Li^+. Accordingly, the obtained $Li_{(5\%)}$-NVO cathode exhibits excellent electrochemical performance: a superior reversible capacity of 486.1 mAh g^{-1} at 0.5 A g^{-1}, a notable capacity of 371.4 mAh g^{-1} at 5 A g^{-1}, and remarkable cycle stability over 5000 cycles, with a capacity retention rate of 72% at 5 A g^{-1}.

2. Results and Discussion

In the present investigation, ammonium metavanadate and oxalic acid dihydrate are used as raw materials to synthesize $NH_4V_4O_{10}$ (NVO) nanosheets by a one-step hydrothermal method. Different proportions of lithium sulfate (0.09, 0.15, 0.21 mmol, equivalent to 3%, 5%, 7% of NH_4VO_3, respectively) are added to the solution to obtain $Li_{(x)}$-NVO (X = 3%, 5%, 7%) samples. Detailed experimental procedures are presented in Supporting Information. From **Figure 1a** and Figure S1 (Supporting Information), the X-ray powder diffraction (XRD) patterns of the $Li_{(x)}$-NVO (X = 0, 3%, 5%, 7%) are well indexed to the monoclinic structure of $NH_4V_4O_{10}$ (JCPDS No. 31–0075), and no peaks associated with secondary phases are detected after the addition of Li^+. From Figure S1 (Supporting Information), it is clearly noted that the crystallinity of the $Li_{(x)}$-NVO reduces gradually with the increase in the level of Li^+, which may give the material more Zn^{2+} migration pathways. From Figure 1b, the strong signal at 2θ = 9.20° is associated with the (001) crystal plane of the NVO with a layer spacing of 9.6 Å, while the diffraction peak of the (001) crystal plane of the material decreases to 9.04°, corresponding to the layer spacing of 9.8 Å, when Li^+ (5%) is introduced to the NVO interlayers. When the Zn^{2+} ion diffuses between layers, larger layer spacing can reduce Coulomb interactions with interlayers. Fourier transform infrared spectroscopy (FTIR) analysis confirms that NVO and $Li_{(5\%)}$-NVO share similar crystal structures (Figure 1c). Peaks observed at 1620 and 3422 cm^{-1} are indicative of bending and tensile vibrations of water, providing evidence for the presence

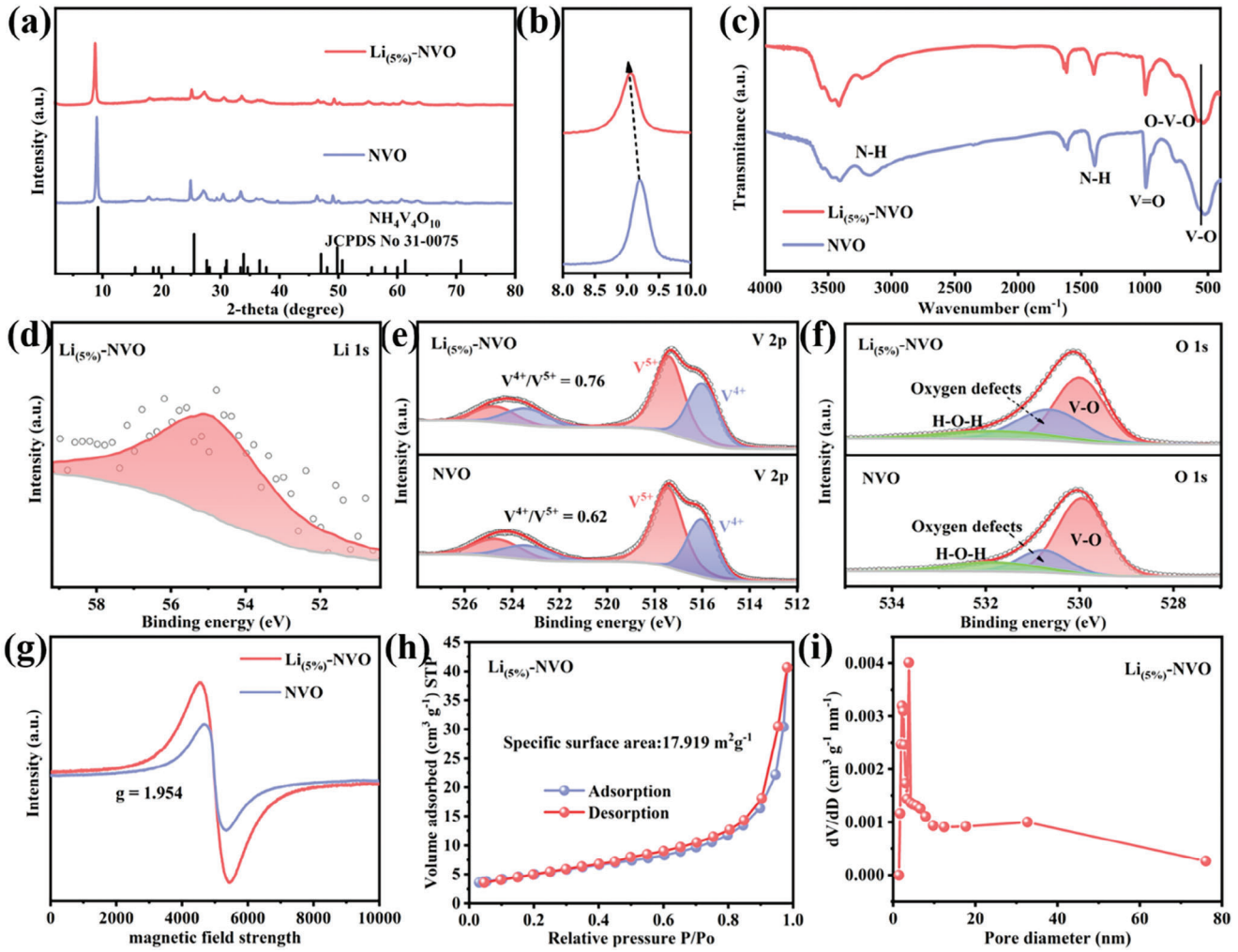

Figure 1. a,b) XRD diagrams of NVO and $Li_{(5\%)}$-NVO. c) FTIR spectra of NVO and $Li_{(5\%)}$-NVO. d) XPS spectrum of Li 1s for $Li_{(5\%)}$-NVO. e) XPS spectra of V 2p and f) O 1s for NVO and $Li_{(5\%)}$-NVO. g) EPR spectra of NVO and $Li_{(5\%)}$-NVO. h) N_2 adsorption/desorption isotherm, and i) the corresponding pore size distribution of $Li_{(5\%)}$-NVO.

of structural water molecules in the material. Peaks at ≈1394 and 3178 cm^{-1} arise from the bending and tensile vibrations of N—H bonds, confirming the existence of NH_4^+. Characteristic peaks at 989, 746, and 520 cm^{-1} in NVO and $Li_{(5\%)}$-NVO materials represent V═O, V—O—V, and V—O with different vibration modes, respectively. The peak at 520 cm^{-1} is attributed to the bending vibration mode of V—O. The blue shift observed in the V—O peak of $Li_{(5\%)}$-NVO is attributed to the generation of oxygen vacancies resulting from the introduction of Li^+. The X-ray photoelectron spectroscopy (XPS) of Li 1s in the $Li_{(5\%)}$-NVO sample verifies the successful insertion of Li^+ (Figure 1d). Furthermore, the inductively coupled plasma-atomic emission spectroscopy (ICP-AES) is used to reveal the composition of the $Li_{(x)}$-NVO. According to the ICP results, the chemical compositions of $Li_{(3\%)}$-NVO, $Li_{(5\%)}$-NVO, and $Li_{(7\%)}$-NVO can be expressed as $Li_{0.12}NH_4V_4O_{10}$, $Li_{0.23}NH_4V_4O_{10}$, and $Li_{0.3}NH_4V_4O_{10}$, respectively (Table S1, Supporting Information). In the V 2p XPS spectra (Figure 1e), the characteristic peaks at 517.5/524.6 eV and 516.1/523.3 eV are indicative of the presence of V^{5+} and V^{4+}, respectively.[46] According to the calculation of the fitted peak areas of V 2p, the proportion of V^{4+}/V^{5+} in the $Li_{(5\%)}$-NVO surpasses that of the NVO. This discrepancy can be attributed to the increased content of oxygen vacancies induced by the insertion of Li^+. Consequently, part of V^{5+} undergoes reduction to V^{4+}. In addition, the XPS spectra of O 1s for the NVO and $Li_{(5\%)}$-NVO are displayed in Figure 1f, which can be fitted into three peaks. The characteristic peaks at 529.9, 530.5 and 531.5 eV represent V—O bonds, oxygen defects and H_2O molecules, respectively. The characteristic peak associated with oxygen vacancies in the $Li_{(5\%)}$-NVO is significantly stronger than that in the NVO, indicating the higher content of oxygen vacancies in the $Li_{(5\%)}$-NVO. The electron paramagnetic resonance (EPR) spectrum provides the proof of the existence of oxygen vacancies. Both the NVO and $Li_{(5\%)}$-NVO materials exhibit symmetric peaks of g = 1.954 (Figure 1g). This phenomenon arises from the interaction between the unpaired electrons of V^{4+} and adjacent O atoms, leading to the generation of oxygen radicals associated with oxygen vacancies. Apparently, the $Li_{(5\%)}$-NVO exhibits a much stronger signal, indicating the

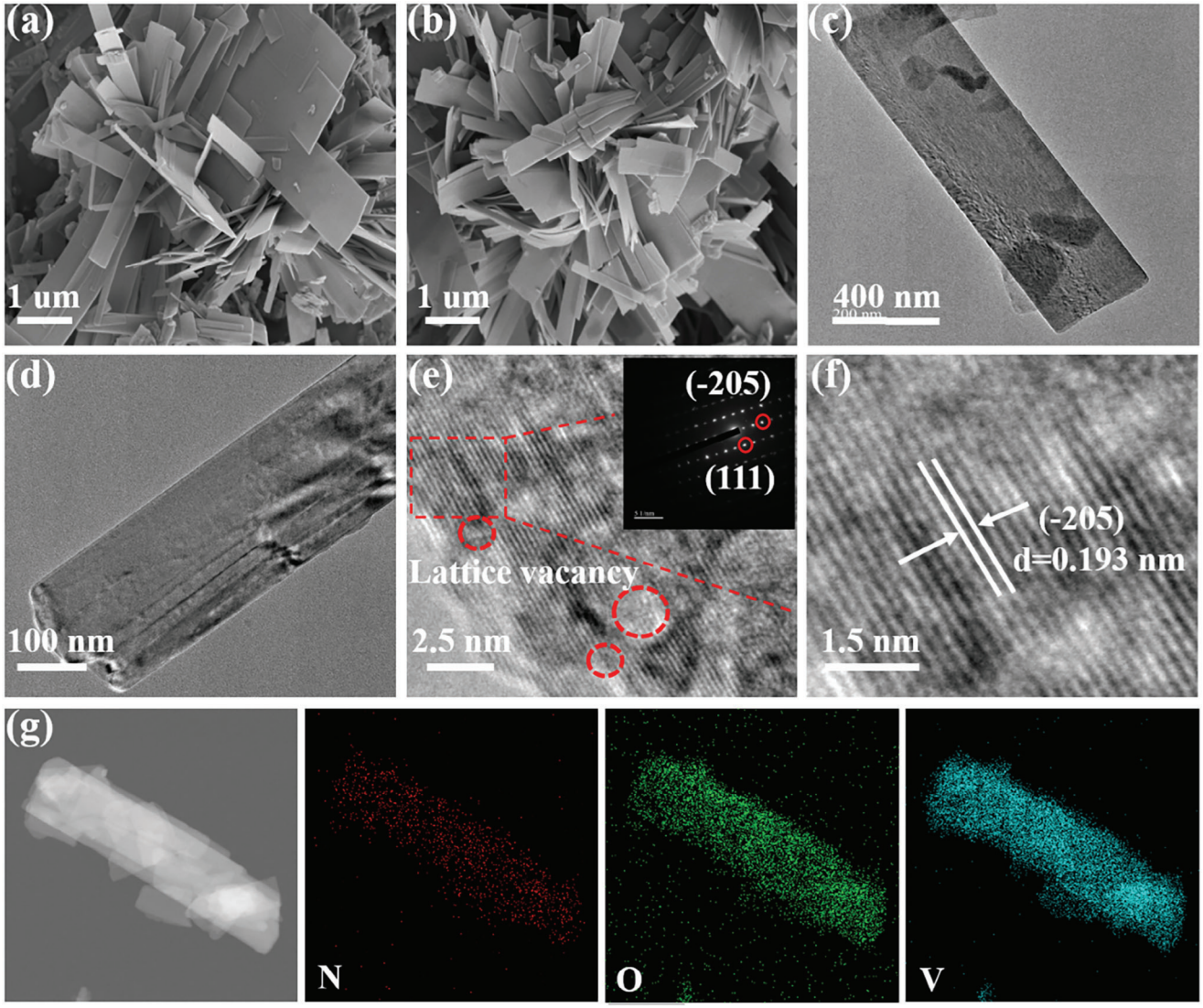

Figure 2. a,b) SEM pictures of $Li_{(5\%)}$-NVO. c,d) TEM pictures of $Li_{(5\%)}$-NVO. e) HRTEM image and SAED spectrum of $Li_{(5\%)}$-NVO. f) Enlarged view of the selected part of the HRTEM image of $Li_{(5\%)}$-NVO. g) Elemental mapping of $Li_{(5\%)}$-NVO.

formation of more oxygen vacancies in the $Li_{(5\%)}$-NVO.[47] The nitrogen adsorption-desorption isotherm and pore size distribution of the materials are shown in Figure 1h,i and Figures S2 and S3 (Supporting Information). The NVO and $Li_{(5\%)}$-NVO are both mesoporous with the pore sizes of ≈2–10 nm. Clearly, the $Li_{(5\%)}$-NVO exhibits a larger specific surface area compared to the NVO, leading to a larger electrochemical interface and enhanced electrolyte penetration during chemical reactions.[48]

The morphology and microstructure of the NVO and $Li_{(X)}$-NVO cathode are characterized by scanning electron microscopy (SEM) and transmission electron microscopy (TEM). From Figure S4 (Supporting Information), the NVO consists of inhomogeneous strips. Fortunately, upon intercalation of Li^+ into the interlayers of the NVO, the $Li_{(X)}$-NVO materials undergo a gradual transformation into an ultra-thin nanosheet morphology. However, an excess Li^+ destroys the micromorphology of nanosheets (**Figure** 2a–d; Figures S5 and S6, Supporting Information). The different hydration radii between Li^+ ions and NH_4^+ ions play a crucial role in altering the growth rate of particles in the precursor system, leading to micromorphological changes from strips to ultra-thin nanosheets. Clearly, the $Li_{(5\%)}$-NVO possesses the most refined ultra-thin nanosheet micromorphology compared to other materials, providing a greater number of active sites and favoring the electrolyte penetration. The high-resolution transition electron microscopy (HRTEM) images of the $Li_{(5\%)}$-NVO reveal various lattice defects caused by oxygen vacancies, along with lattice fringes of 0.193 nm, corresponding to the (−205) crystal plane of NVO (Figure 2e,f). The corresponding selective area electron diffraction (SAED) for the $Li_{(5\%)}$-NVO reveals the single-crystal nature of the $Li_{(5\%)}$-NVO. From the element mapping in Figure 2g, the N, O, and V elements are evenly distributed throughout the nanosheet of the $Li_{(5\%)}$-NVO.

To analyze the electrochemical properties of the NVO and $Li_{(X)}$-NVO, coin-type batteries are assembled with zinc foil as the

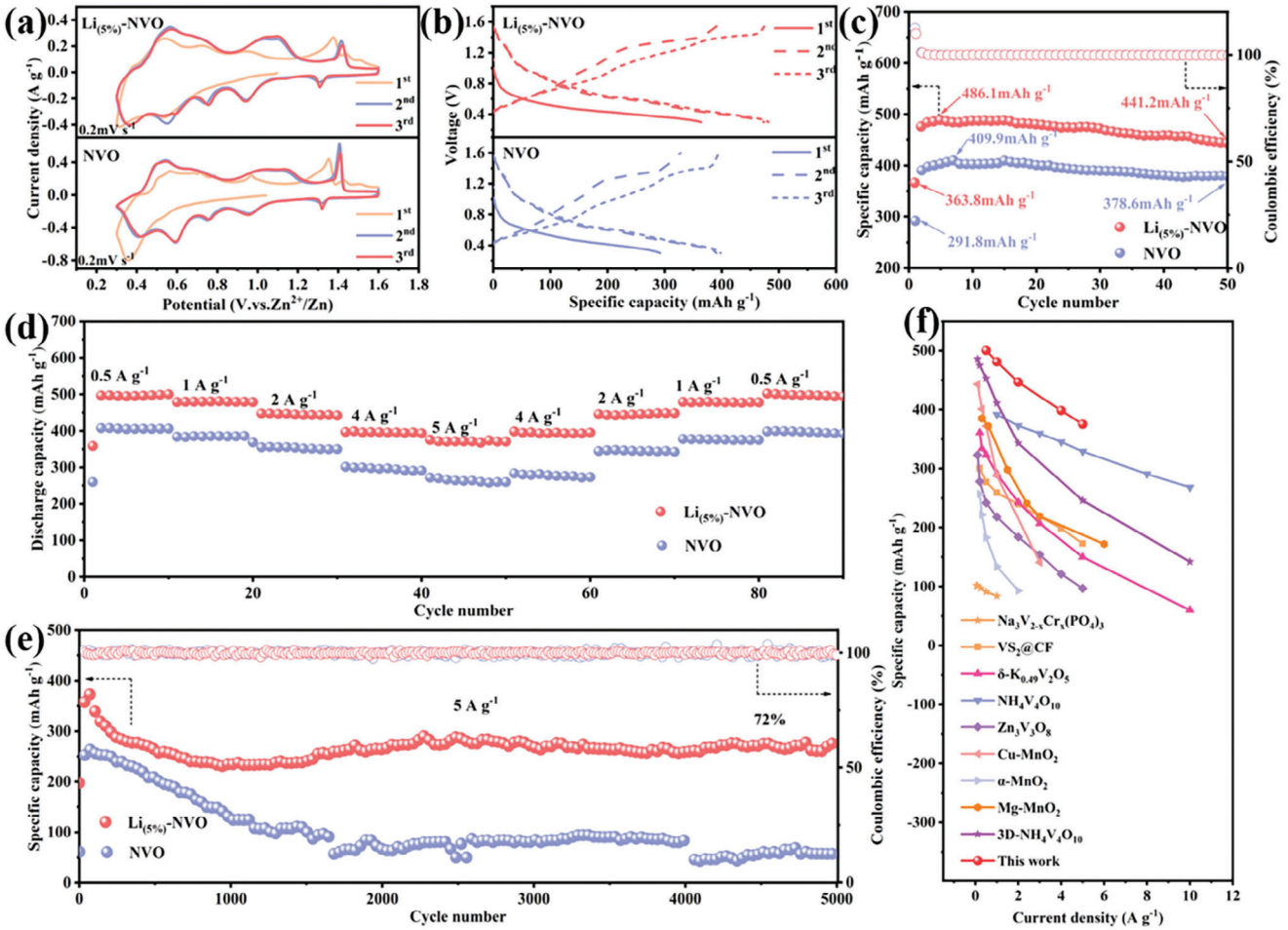

Figure 3. a) CV and b) GCD curves of NVO and $Li_{(5\%)}$-NVO. c) Cycling stability of NVO and $Li_{(5\%)}$-NVO at 0.5 A g^{-1}. d) Rate performance of NVO and $Li_{(5\%)}$-NVO. e) Cycling performance of NVO and $Li_{(5\%)}$-NVO (12:1) at 5 A g^{-1}. f) Comparison of rate performance $Li_{(5\%)}$-NVO with recently reported cathodes for AZIBs.

anode, NVO and $Li_{(X)}$-NVO as the cathodes, and $Zn(CF_3SO_3)_2$ as the electrolyte. **Figure 3a** shows the first three cycles of the NVO and $Li_{(5\%)}$-NVO electrodes, where the voltage range and scanning rate are set at 0.3–1.6 V and 0.2 mV s^{-1}, respectively. Evidently, all the cyclic voltammetry (CV) curves exhibit four similar redox peaks at 1.11/0.94 V, 1.04/0.76 V, 0.57/0.52 V and 0.38/0.35 V, respectively. These peaks correspond to the multi-step behaviors of intercalation/deintercalation of Zn^{2+} during charge and discharge.[31,38,42] Notably, the reaction involving V^{4+}/V^{3+} occurs at ≈0.5 V, while the peak value at a higher voltage of ≈1 V is associated with the redox of V^{5+}/V^{4+}.[49–52] Another small redox peaks at 1.42/1.30 V may be attributed to Zn^{2+} intercalation/deintercalation into/from the $Zn_3(OH)_2V_2O_7{\cdot}2H_2O$ phase formed during cycling.[53,54] From Figure 3b,c and Figure S7 (Supporting Information), the $Li_{(5\%)}$-NVO cathode exhibits superior electrochemical reactivity, yielding the largest reversible capacities and optimal cycling stability. At 0.5 A g^{-1}, the $Li_{(5\%)}$-NVO cathode shows an initial discharge specific capacity of 363.8 mAh g^{-1}, but its discharge capacity increases significantly to 486.1 mAh g^{-1} after 4 cycles (NVO: 400.9 mAh g^{-1}; $Li_{(3\%)}$-NVO: 455.1 mAh g^{-1}; and $Li_{(7\%)}$-NVO:452 mAh g^{-1}), and the capacity retention rate is even 91% after 50 cycles. The discharge capacities of the $Li_{(5\%)}$-NVO cathode are 496.7, 478.8, 447.4, 396.8 and 375.2 mAh g^{-1} at current densities of 0.5, 1, 2, 4 and 5 A g^{-1}, respectively, while the discharge capacities return to 398.2, 445.5, 479.2 and 501.9 mAh g^{-1} when the current densities are restored to 4, 2, 1 and 0.5 A g^{-1}, respectively (Figure 3d). Compared to the NVO cathode (407.6, 383.8, 355.1, 301.4, and 271.6 mAh g^{-1} at 0.5, 1, 2, 4 and 5 A g^{-1}, respectively) and other samples ($Li_{(3\%)}$-NVO: 473.8, 457.4, 416.8, 319.2 and 271.1 mAh g^{-1} at 0.5, 1, 2, 4 and 5 A g^{-1}, respectively; and $Li_{(7\%)}$-NVO: 463.7, 445.9, 410.1, 369.7 and 349.8 mAh g^{-1} at 0.5, 1, 2, 4 and 5 A g^{-1}, respectively) (Figure S8, Supporting Information), the $Li_{(5\%)}$-NVO exhibits much better rate performance across a range of current densities. In addition, the $Li_{(5\%)}$-NVO cathode provides a superior discharge specific capacity of 371.4 mAh g^{-1} at a high current density of 5 A g^{-1}. From Figure 3e, the $Li_{(5\%)}$-NVO provides a capacity of 268.5 mAh g^{-1} with a capacity retention rate of 72% even after 5000 cycles. In contrast, the NVO, $Li_{(3\%)}$-NVO, and $Li_{(7\%)}$-NVO exhibit the low capacities of 260.3, 344.7, and 342.8 mAh g^{-1} with poor capacity retention rates of 23%, 53% and 42% after 5000 cycles, respectively (Figure S9, Supporting Information).

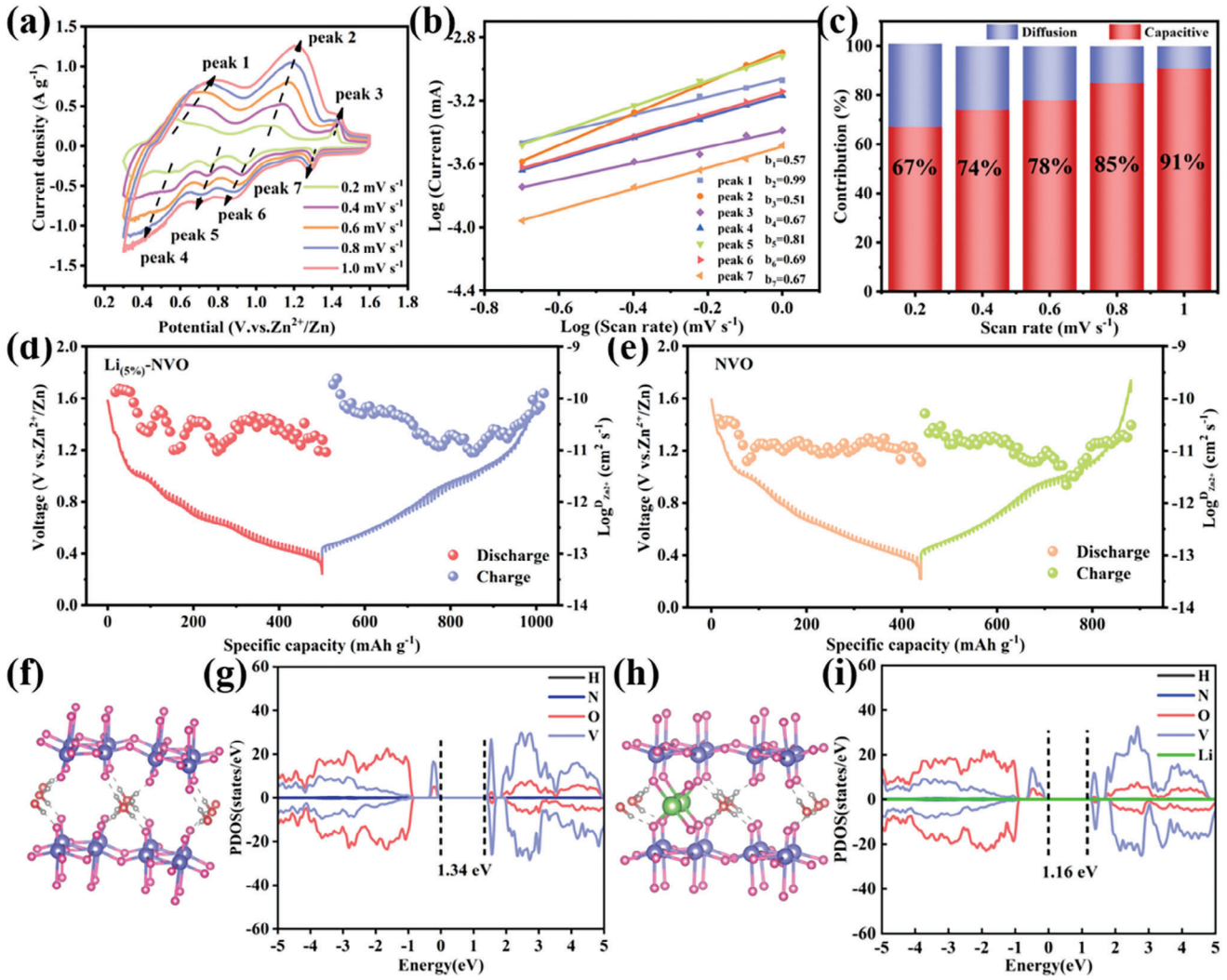

Figure 4. a) CV curves of $Li_{(5\%)}$-NVO electrode. b) log(*i*) versus log(*v*) plots of $Li_{(5\%)}$-NVO electrode. c) Capacitive contributions of $Li_{(5\%)}$-NVO at various scan rates. GITT curves at 0.1 A g^{-1} and Zn^{2+} diffusion coefficient ($D_{Zn}{}^{2+}$) of d) $Li_{(5\%)}$-NVO and e) NVO. First-principle calculations results: optimized geometry structures of f) NVO and h) $Li_{(5\%)}$-NVO, and partial density of states (PDOS) of g) NVO and i) $Li_{(5\%)}$-NVO.

The $Li_{(5\%)}$-NVO electrode achieves a peak capacity of 270 mAh g^{-1} at 10 A g^{-1}, maintaining a high capacity retention rate of 95% after 2000 cycles. This further demonstrates the excellent cycling performance of the electrode, particularly at high current densities. (Figure S10, Supporting Information) In addition, the electrochemical performance of cathode materials for AZIBs is summarized in Figure 3f and Table S2 (Supporting Information), reflecting the superiority of the prepared $Li_{(5\%)}$-NVO cathode compared to other recently reported cathodes of AZIBs.[16,28,29,40,55–60]

The electrochemical kinetic behaviors of the $Li_{(5\%)}$-NVO and NVO cathodes are investigated by the CV curves at varied scan rates (0.2–1.0 mV s^{-1}) (**Figure** 4a; Figure S11, Supporting Information). As the scanning rate increases, the CV curves retain a consistent shape. The correlation between maximum current (*i*) and scanning speed (*v*) can be expressed by $i = av^b$, where the value of b ranges from 0.5 to 1. When b is close to 0.5, the storage mechanism of Zn^{2+} is controlled by diffusion, whereas if b is close to 1, the storage mechanism of Zn^{2+} is governed by a pseudocapacitance process.[61–63] From Figure 4b and Figure S12 (Supporting Information), the b values of peaks 1–7 for the $Li_{(5\%)}$-NVO and NVO cathodes are 0.57, 0.99, 0.51, 0.67, 0.81, 0.69 and 0.67, and 0.64, 0.99, 0.51, 0.75, 0.64, 0.74 and 0.81, respectively, suggesting that the charge storage mechanism of the $Li_{(5\%)}$-NVO and NVO cathodes is jointly controlled by both diffusion and pseudocapacitance characteristics. Moreover, the pseudocapacitance and diffusion contributions are further quantified according to the formula of $i(v) = k_1v + k_2v^{1/2}$. Among them, k_1v indicates the pseudocapacitance contribution, while $k_2v^{1/2}$ indicates the diffusion control contribution. Figure 4c and Figure S13 (Supporting Information) show that when the scanning speed is promoted from 0.2 to 1.0 mV s^{-1}, the pseudocapacitance contribution of the $Li_{(5\%)}$-NVO cathode increases from 67% to 91%, which is much higher than the NVO cathode (65% to 85%). The GITT test provides more evidence for the Zn^{2+} diffusion kinetics of the $Li_{(5\%)}$-NVO and NVO cathodes (Figures 4d,e). It can be seen that the Zn^{2+} diffusion coefficient of the $Li_{(5\%)}$-NVO electrode

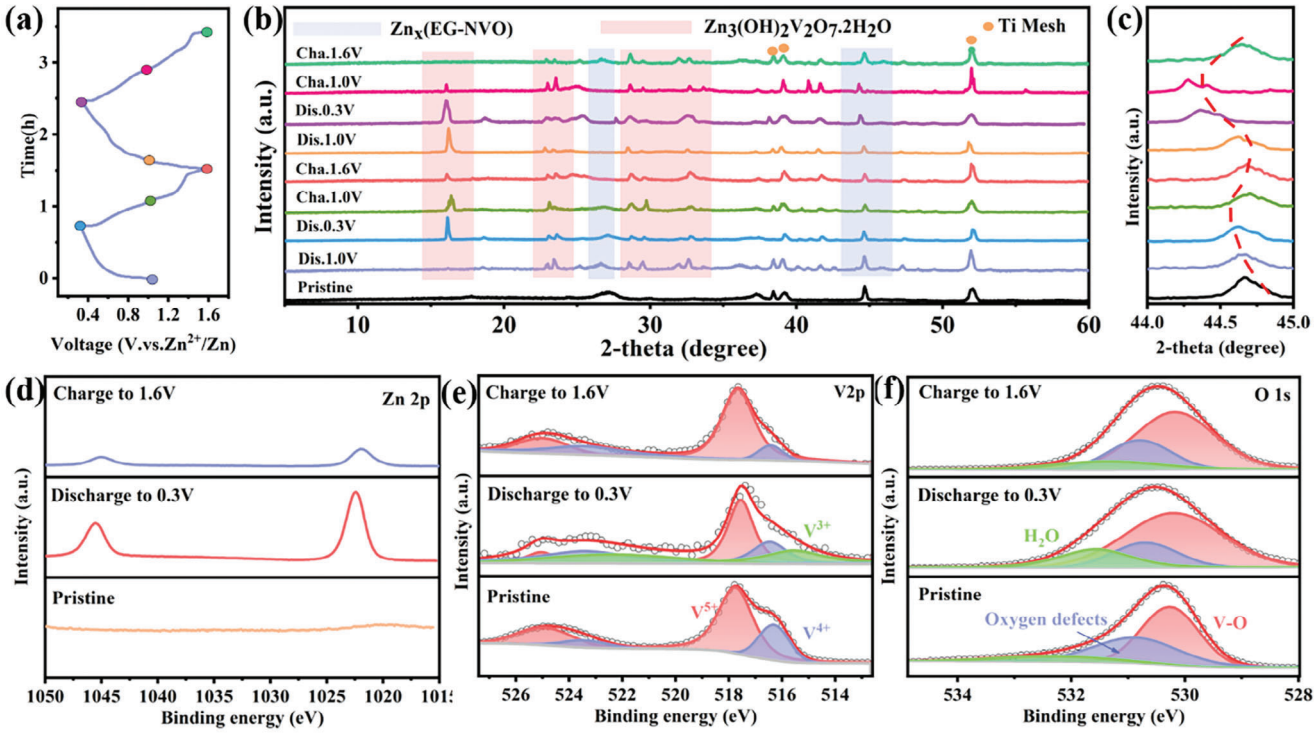

Figure 5. a–c) Ex situ XRD patterns and GCD curves of $Li_{(5\%)}$-NVO electrode. Ex situ XPS spectra for d) Zn 2p, e) V 2p, and f) O 1s of $Li_{(5\%)}$-NVO cathode.

(10^{-9}–10^{-11} cm^2 s^{-1}) is an order of magnitude higher than that of the NVO (10^{-10}–10^{-12} cm^2 s^{-1}). Figure S14 (Supporting Information) shows the electrochemical impedance spectra (EIS) of the $Li_{(5\%)}$-NVO and NVO. The semicircle in the high-frequency region represents the interfacial charge transfer resistance (R_{ct}), while the diagonal in the low-frequency region is related to ion diffusion. Clearly, the charge transfer impedance of the $Li_{(5\%)}$-NVO (214 Ω) is significantly smaller compared to the NVO (312 Ω) electrodes, indicating that the $Li_{(5\%)}$-NVO has faster charge transfer. A linear regression analysis is conducted to establish the relationship between Z_{re} and $\omega^{-1/2}$, and the slopes of the $Li_{(5\%)}$-NVO and NVO electrodes are found to be 11.71 and 48.85, respectively, and the diffusion coefficients are 10^{-9}–10^{-11} cm^2 s^{-1} and 10^{-10}–10^{-12} cm^2 s^{-1}, respectively, which further verify that the $Li_{(5\%)}$-NVO possesses better ion transfer kinetics. (Table S3, Supporting Information).

To further investigate the electronic effect of introducing Li^+ into the NVO, density functional theory (DFT) calculations are performed. The optimized geometry structures and partial density of states (PDOS) of NVO and Li-NVO are shown in Figure 4f–i. In comparison to the NVO, Li-NVO exhibits several new electron states near the Fermi level, and its band gap undergoes a significant reduction from 1.34 to 1.16 eV. This reduction indicates a notable improvement in the conductivity of Li-NVO after the introduction of Li^+, which is more conducive to the efficient transfer of electrons during redox reactions, thereby enhancing the electrochemical activity of the materials.

To comprehend the charge storage mechanism of the $Li_{(5\%)}$-NVO, the electrode at the designated states is examined through ex situ XRD, ex situ XPS and ex situ SEM, and the results are shown in **Figure 5** and Figures S15–S19 (Supporting Information). Figure 5a–c presents the phase evolution of the $Li_{(5\%)}$-NVO at different charging and discharging states examined by ex situ XRD. The change in the layer spacing of the $Li_{(5\%)}$-NVO is evaluated by amplifying the diffraction peak at 44.6° (Figure 5c). In the initial discharge process, the diffraction peak gradually shifts toward a lower angle, which is attributed to the increase in the layer spacing of the $Li_{(5\%)}$-NVO material with the embedding of Zn^{2+}. In addition, during subsequent discharge, the voltage gradually decreases to 0.3 V, and new diffraction peaks appear at ≈16.1°, 23°, and 28.6°, corresponding to the formation of the $Zn_3(OH)_2V_2O_7{\cdot}2H_2O$ (JCPDS: 50–0570) phase, which is a common by-product of V-based materials during electrochemical reactions for AZIBs.[31,38,39,64,65] From ex situ SEM images after complete discharge (Figures S15 and S16, Supporting Information), a large number of flakes are generated, further confirming the appearance of by-products. Instead, when the voltage slowly returns to 1.6 V during charging, the diffraction peak is gradually back to its initial position as Zn^{2+} ions are removed from the $Li_{(5\%)}$-NVO cathode, indicating a reduction in layer spacing. Simultaneously, the intensity of the diffraction peak corresponding to $Zn_3(OH)_2V_2O_7{\cdot}2H_2O$ is significantly weakened, and an obvious decrease in the number of flakes is observed by SEM (Figure S17, Supporting Information). Throughout the subsequent charge–discharge cycles, similar shift in the diffraction peak occurs alongside the appearance and disappearance of by-products (Figures S18 and S19, Supporting Information).

The changes in V valence state, Zn and H_2O contents during charge and discharge are further studied by ex situ XPS.[66] As illustrated in Figure 5d, there is no Zn 2p signal in its original

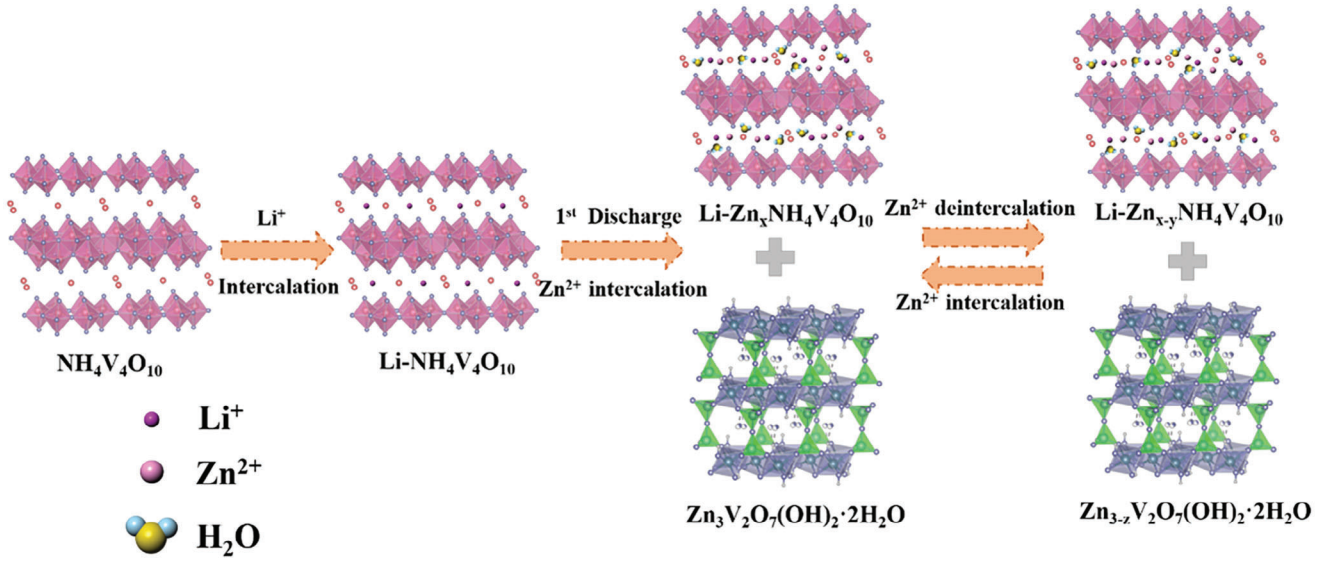

Figure 6. Schematic representation of the Zn^{2+} ion storage mechanism in Li-NVO.

state. Then, in the first fully discharged state, two peaks emerge at ≈1045 and 1022 eV, verifying the successful insertion of Zn^{2+}. Meanwhile, in the fully charged state, the strength of the Zn signal diminishes significantly due to the extraction of Zn^{2+} ions. However, the presence of residual electrolyte and the incomplete disappearance of $Zn_3(OH)_2V_2O_7{\cdot}2H_2O$ (JCPDS: 50–0570) contribute to the continued existence of the Zn signal. The XPS spectra of V 2p are shown in Figure 5e. Compared to the initial state, a new V^{3+} peak becomes apparent in the fully discharged V 2p spectra. Meanwhile, the peak areas of V^{5+} and V^{4+} reduce, indicating a reduction of the valence state of V attributed to the insertion of Zn^{2+}. Upon raising the voltage to 1.6 V, the V^{3+} peak disappears entirely, and the V 2p spectra resemble the initial state, suggesting a reversible oxidation of V. From the XPS spectra of O 1s (Figure 5f), a significant increase in the proportion of H_2O molecular area is observed when fully discharged to 0.3 V. After charging to 1.6 V, accompanied by the extraction of Zn^{2+}, the peak representing H_2O molecules weakens, implying the involvement of both water molecules and Zn^{2+} in the intercalation process. The XPS spectra of the electrode materials before and after cycling reveal that characteristic Li^+ ion peaks persist in the materials, even after the charging and discharging processes, affirming the stable presence of Li^+ ions. (Figure S20, Supporting Information).

According to the characterizations and analyses of above ex situ tests, the schematic illustration of the conversion of the cathode material during the charge and discharge process is depicted in **Figure 6**. To provide a clear understanding of the Zn^{2+} storage mechanism during electrochemical reactions, the electrode reactions involved are as follows:

First discharge on cathode:

$$Li - NH_4V_4O_{10} + nZn^{2+} + 2ne^- \rightarrow Li - Zn_xNH_4V_4O_{10} + Zn_3V_2O_7(OH)_2 \cdot 2H_2O \quad (1)$$

The following cycle on cathode:

$$Li - Zn_xNH_4V_4O_{10} + Zn_3V_2O_7(OH)_2 \cdot 2H_2O - (y+z)\,Zn^{2+} - 2(y+z)\,e^- \leftrightarrow Li - Zn_{x-y}NH_4V_4O_{10} + Zn_{3-z}V_2O_7(OH)_2 \cdot 2H_2O \quad (2)$$

3. Conclusion

In this work, Li^+ pre-intercalated $NH_4V_4O_{10}$ ultrathin nanosheets have been developed by a simple one-step solvothermal method as high-performance cathode materials for AZIBs. Compared to the NVO, the $Li_{(5\%)}$-NVO cathodes offer high capacity (486.1 mAh g^{-1} at 0.5 A g^{-1}) and excellent cycling stability (72% capacity retention over 5000 cycles at 5 A g^{-1}). The excellent electrochemical performance of $Li_{(5\%)}$-NVO electrode can be attributed to the synergistic effect of Li^+ pre-intercalation, which regulates the interplanar spacing, oxygen vacancies, and micromorphology of the NVO. It is found that pre-inserting Li^+ into NVO leads to an expansion of the interlayer distance to 9.8 Å. This expansion creates large interlaminar channels for Zn^{2+} (de)intercalation. Simultaneously, Li^+ intercalation weakens the crystallinity of the material, induces the micromorphological transformation from non-nanostructured strips to ultrathin nanosheets, and increases the level of oxygen defects, which facilitate the exposure of more active sites for ion and electron transport, promote electrolyte penetration, and improve the electrochemical kinetics for the electrode. Moreover, the intercalation of Li^+ generates new electron states near the Fermi level, thereby enhancing the conductivity of material and electron transfer in redox reactions. This investigation serves as a useful reference for synthesizing high-performance cathodes for AZIBs through the synergistic regulation of interplanar spacing, oxygen vacancies, and micromorphology in layer-structured vanadium-based compounds.

Supporting Information

Supporting Information is available from the Wiley Online Library or from the author.

Acknowledgements

This work was supported by National College Students' innovation and entrepreneurship training program (202310636004), Natural Science Foundation of Sichuan Province (2022NSFSC0222) and Sichuan Science and Technology Program (2023NSFSC0439). The authors gratefully acknowledge HZWTECH for providing computation facilities. The authors also appreciate the Shiyanjia Lab (www.shiyanjia.com) for the SEM tests, eceshi (www.eceshi.cn) for the TEM tests and Beijing Nordson Rongke Technology Co., Ltd (www.kexingtest.com) for the BET tests.

Conflict of Interest

The authors declare no conflict of interest.

Data Availability Statement

The data that support the findings of this study are available from the corresponding author upon reasonable request.

Keywords

aqueous zinc-ion batteries, cathode, lithium ion, $NH_4V_4O_{10}$, pre-insertion

Received: October 17, 2023
Revised: January 16, 2024
Published online:

[1] X. Zhang, J. Chen, H. Cao, X. Huang, Y. Liu, Y. Chen, Y. Huo, D. Lin, Q. Zheng, K.h. Lam, *Small.* **2023**, *19*, 2303906.
[2] T. Koketsu, J. Ma, B. J. Morgan, M. Body, C. Legein, W. Dachraoui, M. Giannini, A. Demortière, M. Salanne, F. Dardoize, H. Groult, O. J. Borkiewicz, K. W. Chapman, P. Strasser, D. Dambournet, *Nat. Mater.* **2017**, *16*, 1142.
[3] E. A. Esparcia, M. S. Chae, J. D. Ocon, S.-T. Hong, *Chem. Mater.* **2018**, *30*, 3690.
[4] Y. An, Y. Tian, K. Zhang, Y. Liu, C. Liu, S. Xiong, J. Feng, Y. Qian, *Adv. Funct. Mater.* **2021**, *31*, 2101886.
[5] H. Cao, X. Huang, Y. Li, Y. Liu, Q. Zheng, Y. Huo, R. Zhao, J. Zhao, D. Lin, *Chem. Eng. J.* **2023**, *455*, 140538.
[6] W. Gong, B. Fugetsu, W. Mao, A. K. Vipin, I. Sakata, L. Su, X. Zhang, M. Endo, *J. Mater. Chem. A.* **2022**, *10*, 15415.
[7] T. Wang, S. Li, X. Weng, L. Gao, Y. Yan, N. Zhang, X. Qu, L. Jiao, Y. Liu, *Adv. Energy Mater.* **2023**, *13*, 2204358.
[8] W. Wang, D. Liu, Y. Jiang, D. Zhang, X. Shen, S. Li, J. Liang, H. Xu, *Chem. Eng. J.* **2023**, *463*, 142309.
[9] Y. Li, J. Chen, L. Su, X. Zhang, Q. Zheng, Y. Huo, D. Lin, *J. Colloid Interface Sci.* **2023**, *652*, 440.
[10] M. S. Javed, H. Lei, Z. Wang, B.-T. Liu, X. Cai, W. Mai, *Nano Energy.* **2020**, *70*, 104573.
[11] D. Chen, H. Chen, C.-F. Du, L. Liu, H. Geng, H. Yu, X. Rui, *J. Mater. Chem. A.* **2022**, *10*, 5479.
[12] L. Deng, X. Niu, G. Ma, Z. Yang, L. Zeng, Y. Zhu, L. Guo, *Adv. Funct. Mater.* **2018**, *28*, 1800670.
[13] L. Hu, Z. Wu, C. Lu, F. Ye, Q. Liu, Z. Sun, *Energy Environ. Sci.* **2021**, *14*, 4095.
[14] X. Wang, Z. Zhang, M. Huang, J. Feng, S. Xiong, B. Xi, *Nano Lett.* **2021**, *22*, 119.
[15] H. Jiang, Y. Zhang, L. Xu, Z. Gao, J. Zheng, Q. Wang, C. Meng, J. Wang, *Chem. Eng. J.* **2020**, *382*, 122844.
[16] Q. Li, X. Rui, D. Chen, Y. Feng, N. Xiao, L. Gan, Q. Zhang, Y. Yu, S. Huang, *Nano-Micro Lett.* **2020**, *12*, 67.
[17] R. Li, F. Xing, T. Li, H. Zhang, J. Yan, Q. Zheng, X. Li, *Energy Storage Mater.* **2021**, *38*, 590.
[18] M. Bao, Z. Zhang, X. An, J. Liu, J. Feng, B. Xi, S. Xiong, *Nano Res.* **2022**, *16*, 2445.
[19] Q. Pang, X. Yu, S. Zhang, W. He, S. Yang, Y. Fu, Y. Tian, M. Xing, X. Luo, *Nanomaterials.* **2021**, *11*, 1429.
[20] Y. Yang, Y. Tang, G. Fang, L. Shan, J. Guo, W. Zhang, C. Wang, L. Wang, J. Zhou, S. Liang, *Energy Environ. Sci.* **2018**, *11*, 3157.
[21] F. Jing, Y. Liu, Y. Shang, C. Lv, L. Xu, J. Pei, J. Liu, G. Chen, C. Yan, *Energy Storage Mater.* **2022**, *49*, 164.
[22] Y. Liu, Z. Qin, X. Yang, X. Sun, *Adv. Funct. Mater.* **2022**, *32*, 2106994.
[23] X. Li, Q. Zhou, Z. Yang, X. Zhou, D. Qiu, H. Qiu, X. Huang, Y. Yu, *Energy Environ. Mater.* **2022**, *6*, 12378.
[24] M. Görlin, D. O. Ojwang, M.-T. Lee, V. Renman, C.-W. Tai, M. Valvo, *ACS Appl Mater Interfaces.* **2021**, *13*, 59962.
[25] Q. Li, K. Ma, C. Hong, Z. Yang, C. Qi, G. Yang, C. Wang, *Energy Stor. Mater.* **2021**, *42*, 715.
[26] Y. Chen, X. Liao, P. Wang, J. Chen, X. Zhang, X. Wu, S. C. Smith, D. Lin, X. Tan, Q. Zheng, *J. Colloid Interface Sci.* **2024**, *653*, 1.
[27] Y. Chen, Q. Li, P. Wang, X. Liao, J. Chen, X. Zhang, Q. Zheng, D. Lin, K.h. Lam, *Small.* **2023**, *19*, 2304002.
[28] K. Wang, H. Li, G. Guo, L. Zheng, S. Passerini, H. Zhang, *ACS Energy Lett.* **2023**, *8*, 1671.
[29] Y. Mao, B. Zhao, J. Bai, H. Ma, P. Wang, W. Li, K. Xiao, S. Wang, X. Zhu, Y. Sun, *Small.* **2023**, *19*, 2207998.
[30] X. Cheng, X. Yang, Y. Zhang, P. Lv, J. Yang, F. Huang, Q. Wei, *Adv. Fiber. Mater.* **2023**, *5*, 650.
[31] B. Tang, J. Zhou, G. Fang, F. Liu, C. Zhu, C. Wang, A. Pan, S. Liang, *J. Mater. Chem. A.* **2019**, *7*, 940.
[32] T. He, Y. Ye, H. Li, S. Weng, Q. Zhang, M. Li, T. Liu, J. Cheng, X. Wang, J. Lu, B. Wang, *Mater. Today.* **2021**, *43*, 53.
[33] J. Chen, L. Su, X. Zhang, Y. Chen, P. Wang, Q. Zheng, D. Lin, *ACS Sustainable Chem. Eng.* **2023**, *11*, 12467.
[34] T.-F. Yi, L. Qiu, J.-P. Qu, H. Liu, J.-H. Zhang, Y.-R. Zhu, *Coord. Chem. Rev.* **2021**, *446*, 214124.
[35] J. Wang, F. Zheng, M. Li, J. Wang, D. Jia, X. Mao, P. Hu, Q. Zhen, Y. Yu, *Chem. Eng. J.* **2022**, *446*, 136922.
[36] G. Li, L. Sun, S. Zhang, C. Zhang, H. Jin, K. Davey, G. Liang, S. Liu, J. Mao, Z. Guo, *Adv. Funct. Mater.* **2023**, *34*, 2301291.
[37] D. He, Y. Peng, Y. Ding, X. Xu, Y. Huang, Z. Li, X. Zhang, L. Hu, *J Power Sources.* **2021**, *484*, 229284.
[38] H. Jiang, Y. Zhang, Y. Liu, J. Yang, L. Xu, P. Wang, Z. Gao, J. Zheng, C. Meng, Z. Pan, *J. Mater. Chem. A.* **2020**, *8*, 15130.
[39] X. Wang, Y. Wang, Y. Jiang, X. Li, Y. Liu, H. Xiao, Y. Ma, Y.y. Huang, G. Yuan, *Adv. Funct. Mater.* **2021**, *31*, 2103210.
[40] Y. Xu, G. Fan, P. X. Sun, Y. Guo, W. Yangyang, X. Gu, L. Wu, L. Yu, *Angew. Chem., Int. Ed.* **2023**, *62*, 202303529.
[41] Q. Zong, Q. Wang, C. Liu, D. Tao, J. Wang, J. Zhang, H. Du, J. Chen, Q. Zhang, G. Cao, *ACS Nano.* **2022**, *16*, 4588.
[42] X. Wang, A. Naveed, T. Zeng, T. Wan, H. Zhang, Y. Zhou, A. Dou, M. Su, Y. Liu, D. Chu, *Chem. Eng. J.* **2022**, *446*, 137090.
[43] Z. Pang, B. Ding, J. Wang, Y. Wang, L. Xu, L. Zhou, X. Jiang, X. Yan, J. P. Hill, L. Yu, Y. Yamauchi, *Chem. Eng. J.* **2022**, *446*, 136861.
[44] J. Gong, S. Yan, Y. Lang, Y. Zhang, S. Fu, J. Guo, L. Wang, G. Liang, *J. Alloys Compd.* **2021**, *859*, 157885.

[45] J. J. Carey, M. Nolan, *J. Mater. Chem. A.* **2017**, *5*, 15613.
[46] Y. Liu, Y. Sun, J. Zhang, X. Hao, M. Zhang, P. Wei, X. Zhao, K. Cai, *Nano Energy.* **2024**, *120*, 109152.
[47] Y. Liu, J. Huang, X. Li, J. Li, J. Yang, K. Cai, *J Energy Chem.* **2023**, *90*, 578.
[48] H. Lu, Z. Zhang, X. An, J. Feng, S. Xiong, B. Xi, *Small Struct.* **2023**, *4*, 2300191.
[49] H. Chen, J. Huang, S. Tian, L. Liu, T. Qin, L. Song, Y. Liu, Y. Zhang, X. Wu, S. Lei, S. Peng, *Adv Sci.* **2021**, *8*, 2004924.
[50] F. Cui, D. Wang, F. Hu, X. Yu, C. Guan, G. Song, F. Xu, K. Zhu, *Energy Stor. Mater.* **2021**, *38*, 389.
[51] H. Tang, F. Chao, H. Luo, K. Yu, J. Wang, H. Chen, R. Jia, F. Xiong, Y. Pi, P. Luo, Q. An, *ChemSusChem.* **2023**, *16*, 202300403.
[52] H. Cao, Z. Zheng, P. Norby, X. Xiao, S. Mossin, *Small.* **2021**, *17*, 2100558.
[53] T. He, S. Weng, Y. Ye, J. Cheng, X. Wang, X. Wang, B. Wang, *Energy Stor. Mater.* **2021**, *38*, 389.
[54] X. Wang, Y. Wang, A. Naveed, G. Li, H. Zhang, Y. Zhou, A. Dou, M. Su, Y. Liu, R. Guo, C. C. Li, *Adv. Funct. Mater.* **2023**, *33*, 2306205.
[55] W. Wang, R. Hu, C. Zhang, Y. Tao, L. Ran, Y. Li, Y. Ouyang, J. Yan, *J. Mater. Chem. A.* **2023**, *11*, 8224.
[56] W. He, C. Meng, Z. Ai, D. Xu, S. Liu, Y. Shao, Y. Wu, X. Hao, *Chem. Eng. J.* **2023**, *454*, 140260.
[57] J. Yang, J. Li, Y. Li, Z. Wang, L. Ma, W. Mai, M. Xu, L. Pan, *Chem. Eng. J.* **2023**, *468*, 143600.
[58] J. Zhang, W. Li, J. Wang, X. Pu, G. Zhang, S. Wang, N. Wang, X. Li, *Angew. Chem., Int. Ed.* **2023**, *62*, 202215654.
[59] Y. Liu, Z. Qin, X. Yang, J. Liu, X.-X. Liu, X. Sun, *Energy Stor. Mater.* **2023**, *56*, 524.
[60] J. Xia, Y. Zhou, J. Zhang, T. Lu, W. Gong, D. Zhang, X. Wang, J. Di, *Small.* **2023**, *19*, 2301906.
[61] S. Zhao, S. Wang, J. Guo, L. Li, C. Li, Y. Sun, P. Xue, D. Wu, L. Wei, Y. Wang, Q. Zhang, *Adv. Funct. Mater.* **2023**, *33*, 2305700.
[62] Q. Zong, Y. Zhuang, C. Liu, Q. Kang, Y. Wu, J. Zhang, J. Wang, D. Tao, Q. Zhang, G. Cao, *Adv. Energy Mater.* **2023**, *13*, 2301480.
[63] M. Zhang, X. Zhang, Q. Dong, S. Zhang, Z. Xu, Z. Hou, Y. Qian, *Adv. Funct. Mater.* **2023**, *33*, 2213187.
[64] H. Wang, R. Jing, J. Shi, M. Zhang, S. Jin, Z. Xiong, L. Guo, Q. Wang, *J. Alloys Compd.* **2021**, *858*, 158380.
[65] R. Sun, Z. Qin, X. Liu, C. Wang, S. Lu, Y. Zhang, H. Fan, *ACS Sustainable Chem. Eng.* **2021**, *9*, 11769.
[66] Q. Hu, J. Hou, Y. Liu, L. Li, Q. Ran, J. Mao, X. Liu, J. Zhao, H. Pang, *Adv. Mater.* **2023**, *35*, 2303336.